Artifacts from manganese reduction in rock samples prepared by focused ion beam (FIB) slicing for X-ray microspectroscopic analysis

Dorothea S. Macholdt[1], Christopher Pöhlker[1], Jan-David Förster[1], Maren Müller[2], Bettina Weber[1], Michael Kappl[2], A. L. David Kilcoyne[3], Markus Weigand[4], Klaus Peter Jochum[1], Meinrat O. Andreae[1,5]

[1]Max Planck Institute for Chemistry, P.O. Box 3060, 55020 Mainz, Germany
[2]Physics of Interfaces Department, Max Planck Institute for Polymer Research, Mainz, Germany
[3]Lawrence Berkeley National Laboratory, Berkeley, CA, United States
[4]Modern Magnetic Systems Department, Max Planck Institute for Intelligent Systems, Stuttgart,   Germany
[5]Geology and Geophysics Department, King Saud University, Riyadh, Saudi Arabia

Correspondence to: Dorothea S. Macholdt (d.macholdt@mpic.com)

Abstract. Manganese (Mn)-rich natural rock coatings, so-called rock varnishes, are discussed controversially regarding their genesis. Biogenic and abiogenic mechanisms, as well as a combination of both, have been proposed to be responsible for the Mn oxidation and deposition process. We conducted scanning transmission X-ray microscopy - near edge X-ray absorption fine structure spectroscopy (STXM-NEXAFS) measurements to examine the abundance and spatial distribution of the different oxidation states of Mn within these nano- to micrometer thick crusts. Such microanalytical measurements of thin and hard rock crusts require sample preparation with minimal contamination risk. Focused ion beam (FIB) slicing, a well-established technique in geosciences, was used in this study to obtain 100-200 nm thin slices of the samples for X-ray transmission spectroscopy. However, even though this preparation is suitable to investigate element distributions and structures in rock samples, we observed that, using standard parameters, modifications of the Mn oxidation states occur in the surfaces of the FIB slices. Based on our results, the preparation technique likely causes the reduction of Mn^{4+} to $Mn^{2+/3+}$. We draw attention to this issue, since FIB slicing, SEM imaging, and other preparation and visualization techniques operating in the keV range are well-established in geosciences, but researchers are often unaware of the potential for reduction of Mn and possibly other elements in the samples' surface layers.

1 Introduction

Rock varnish, an up to about 250 µm thin natural crust on rock surfaces, typically consists of 5-20 % Mn oxyhydroxide minerals, which cement mineral dust grains to produce a hard black coating. Even though a very large number of publications is available about rock varnish, the process of Mn oxidation and precipitation of the matrix is still under debate. In view of this controversy and the scarcity of information on the microchemistry of these varnishes, we conducted several STXM-NEXAFS measurements to investigate not only carbon distributions and functional groups within this material, but also the Mn oxidation states and their distribution. Varnish often consists of layers with different manganese/iron (Mn/Fe) ratios, which are a few tens up to a few hundreds of nanometers thick (Garvie, Burt and Buseck 2008, Krinsley, Dorn and

Tovey 1995)(Macholdt et al., 2017) resembling sedimentary features. It has been assumed that this layering results from variations in the mass fraction of Mn, which initially precipitates homogeneously in the same oxidation state. However, since the genesis of varnish and the precipitation process of the Mn oxyhydroxides are still under debate, this remains an assumption until it can actually be verified. The oxidation state of Mn could have changed subsequent to its deposition, e.g.,

5   due to the presence of reduced iron (Fe^{2+}), since Mn oxyhydroxides are known to be amongst the strongest occurring natural oxidizers and element scavengers (Tebo et al. 2005). Nevertheless, reduced iron, as well as other reduced elements that tend to oxidize rather easily, are scarce in the oxic environment of the upper continental crust (UCC). Another process potentially reducing Mn^{4+} is photoreduction, supported by available organic matter (OM) as electron supply. Photoreduction occurs due to the abundance of narrow band gaps that are present in all Mn oxyhydroxides (Sherman 2005). This process effectuates the

10   dissolution of the solid Mn oxyhydroxide minerals by reduction of immobile Mn^{4+} to Mn^{3+} and further to mobile Mn^{2+}. In most cases the released Mn^{2+} is re-adsorbed to the Mn oxyhydroxide surface instead of being released into the surroundings. The initial idea of this study was to check whether Mn oxidation states provide any information about the genesis of varnish or reveal features that cannot be simply obtained from element distribution mapping.

To investigate the samples with X-ray microspectroscopy, they must be thin enough to transmit at least 10 % of the soft X-

15   ray photons (Cosmidis and Benzerara 2014). To obtain such ultra-thin samples, focused ion beam (FIB) slices were prepared using a gallium ion (Ga^+) sputtering technique. We chose soft X-rays for our STXM-NEXAFS work, since they generate comparatively low radiation damage, provide a high penetration depth (Guttmann and Bittencourt 2015), and have the potential to investigate, in addition to OM, the L-shell absorption of high-Z elements using a high photon flux on a small spot (Cosmidis and Benzerara 2014). In STXM, small measurement spots are produced by an achromatic zone plate (ZP)

20   lens with a focal length proportional to the photon energy, which is mounted in the optical path between the monochromator and the sample (Moffet 2011). The order sorting aperture (OSA), located between the ZP and the sample, filters the light in order to transmit only the positive first diffraction order (Moffet 2011). Measurements provide images that are energy-specific, as well as image sequences at many energy values (so-called stacks). These stacks produce 3D matrices where each pixel contains information about the absorption of all energies measured at this point. The absorption spectra can be

25   extracted from any pixel or group of pixels of a stack, subsequent to subtracting the background signal. They contain information about binding situations and oxidation states, expressed as the exact energies of the absorption edges. The detector converts incoming X-rays to visible light via a phosphor screen (Kilcoyne et al. 2003). The generated visible photons are counted by a high performance photomultiplier (PMT) with counting capabilities in the range of tens of MHz (Kilcoyne et al. 2003).

30   Fourteen different rock varnish samples, containing diverse structures and compositions, from different environments and locations worldwide were investigated in the course of our study. The sample preparation was conducted by FIB, which was used to avoid contamination and to allow preparing samples thin enough to transmit soft X-rays. For these reasons, we chose this preparation technique, even though several weaknesses of this method have already been described. It is, for instance, well-known that FIB slicing does implant Ga^+ ions during the sputtering process (Balcells et al. 2008, Cairney, Smith and

Munroe 2000, Prenitzer et al. 1998, Rubanov and Munroe 2001) and thus creates Ga-rich phases with Ga fractions of up to 20 wt % in the damage region (Susnitzky and Johnson 1998) and up to 30 % in the redeposition layer (Rajsiri et al. 2002), which can melt at low temperatures (Li and Liu 2017). The milled material, which is supposed to become fully removed, might re-deposit on the surface in some cases (Rajsiri et al. 2002). Additionally, surface layers can change and form a thin

5   amorphous film (Bassim et al. 2012, Bender and Roussel 1997, Mardinly and Susnitzky 1998, Siemons et al. 2014), due to the high energy of the Ga^+ ions. This amorphous film is a 20-30 nm thick surface damage layer, when using 30 keV (Giannuzzi, Geurts and Ringnalda 2005, Rubanov and Munroe 2004a, Rubanov and Munroe 2004b), or can become even 50 nm thick, thus in the range of the Ga^+ ion implantation depth, for semiconductor materials (Mayer et al. 2007, Rubanov and Munroe 2004a). However, by reducing the FIB beam voltage from 30 keV to 6-10 keV the thickness of the amorphous layer

10 is reduced by a factor of two (Jamison et al. 2000, Rubanov and Munroe 2001).

Within this affected layer, FIB can generate microstructural modifications in metals and ceramics (Mayer et al. 2007, Michael 2006, Siemons et al. 2014) such as in manganite thin films (Balcells et al. 2008, Pallecchi et al. 2008). Also, FIB can result in reduced crystallinity of the material by generating point defects such as vacancies, interstitials, antisite defects, etc., due to charging effects (Li and Liu 2017, Siemons et al. 2014). This might result in the loss of the long-range order

15 when the density of point defects reaches a critical value (Cerva and Hobler 1993). The amorphisation coincides with heating of the outer sample surface to a few hundred degrees while examining the thin slice by scanning electron microscopy (SEM). Using an incident energy between 500 eV and 2 keV causes heating of the samples to 30 °C and 71 °C, respectively (Li 2003). The temperature can even rise to above 121°C during final thinning after the lift-out phase (Li and Liu 2017). However, only temperatures above about 60 °C are likely to change the material investigated in our study, since rock varnish

20 is known to have been already exposed to high temperatures in desert environments, such as up to 57 °C in Death Valley (Roof and Callagan 2003).

Furthermore, damage during sample observation might emerge from the electron excitation by SEM imaging. During de-excitation, molecules may not return into their original electronic states, but chemical bonds may break, changing the molecule's structure, shifting their position, and causing a loss of crystallinity (Egerton, Li and Malac 2004, Henderson and

25 Glaeser 1985). However, the critical energy needed for the destruction of the electron-diffraction pattern of many organic materials ranges around ~60 keV or more (Reimer 1975). Mass loss or mass gain of organics due to polymerization by incoming or outgoing electrons might occur as well (Egerton et al. 2004). Other options for a modification during SEM imaging are radiolysis through inelastic scattering of electrons, in the case of transition-metal oxides via the Knotek-Feibelman mechanism (Egerton et al. 2004, Knotek and Feibelman 1978), knock-on displacement damage by high-energy

30 electrons of the SEM (Rubanov and Munroe 2004a, Rubanov and Munroe 2004b), and reduction by Auger electron loss (Egerton et al. 2004). All these processes mainly affect the immediate surface of the sample. Direct reduction of Cr^{6+} by X-ray photoelectron spectroscopy analysis has also been observed before (Halada, Clayton and Lindsley 1988).

Here we report about our findings observed during the investigation of the Mn oxidation states in 14 rock varnish samples, collected in different environments and countries. The oxidation states were examined by X-ray microspectroscopy, to gain

insight into oxidation, precipitation, and remobilization processes in the varnishes. In course of our study we repeatedly observed measurement artifacts, independent of the type or origin of varnish examined. For the sake of brevity, and since all samples showed the same phenomena, these findings will be exemplified using measurements on one of the samples; other sample data can be provided upon request.

2 Materials and methods

2.1 Focused ion beam preparation

Since rock varnishes are hard materials, sample preparation was performed using the lift-out FIB technique. This slicing technique was chosen since it is relatively contamination-free (except for gallium $(Ga)^+$ ion implantation), relatively fast, and allows a precise selection of the preparation target area independent of the nature of the sample material or combination of materials (Mayer et al. 2007, Siemons et al. 2014). The preparation was performed at the Max Planck Institute for Polymer Research, Mainz, Germany, using an FEI Nova600Nanolab FIB dual-beam instrument (ThermoFisher Inc.). Simultaneously, SEM was applied to carefully determine and monitor the site of milling (2-5 keV). Before introduction of the objects into the FIB, the entire samples were sputtered with 50 nm of platinum (Pt) using a Baltec MED020 sputtering equipment. Selected sites were coated within the FIB with an additional, approximately 2 μm thick Pt layer using beam-induced Pt deposition from a metallo-organic precursor gas (1 nA at 30 kV). Milling was performed by Ga^+-ion sputtering with a resolution of about 10 nm. In a first milling step (20 nA, 30 kV), two trenches on both sides of the Pt deposition were created, followed by a second milling step at lower beam currents (7 nA and 5 nA at 30 kV) to obtain flat surfaces of the pre-thinned, about 1 μm thick, lamella. After the samples were lifted out and transferred to a TEM grid, onto which they were attached with Pt to allow measurements by STXM-NEXAFS, stepwise final thinning and polishing (1 nA and 0.5 nA at 30 kV) was conducted to produce FIB slices with thicknesses of about 100–200 nm. Thinning was conducted from the top of the sample downwards, four to five times from each side, with decreasing currents. To ensure the sample stability, several samples were divided into two halves, one of which was thinned out stronger than the other (Fig. 1). Since the samples are natural inhomogeneous sediments, and the compositions, the densities, and stabilities are changing over the profiles, some areas thin out faster than others. This effect produced an artificial hole in the sample that we want to show in the following as example. The hole formed where the sample was thinned out so strongly that the material was fully removed, providing us with an excellent thickness gradient to study in the following.

Geoscientific
Instrumentation
Methods and
Data Systems
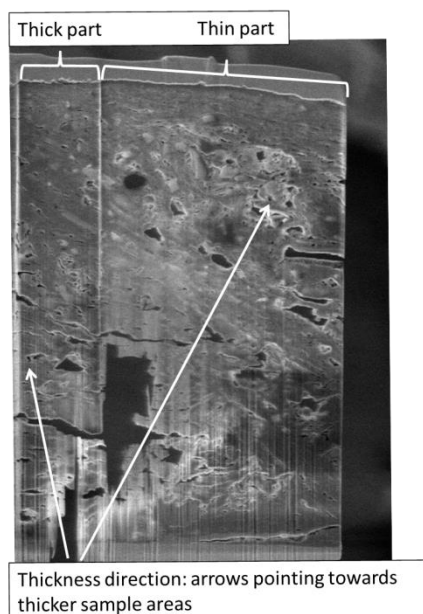
Open Access

Discussions

EGU

Figure 1: FIB slice of rock varnish sample AR14-J01 collected in Saudi Arabia. Arrows indicate the sample thickness. The sample becomes thicker towards the head of the arrow. At the left side, the sample remained thicker.

2.2 Scanning transmission X-ray microscopy - near edge X-ray absorption fine structure spectroscopy

Subsequent to the preparation by FIB, the samples were studied using two STXM-NEXAFS instruments. One instrument is located at beamline 5.3.2.2 of the Advanced Light Source (ALS) in Berkeley, California (Kilcoyne et al. 2003). It is equipped with a bending magnet and allows measurements in the energy range between 250 eV and 800 eV. The second instrument, MAXYMUS, is located at beamline UE46-PGM-2 of BESSY II in the Helmholtz-Zentrum Berlin, Germany (Follath et al. 2010, Weigand 2015). It is equipped with an undulator and allows measurements in the effective energy range between 250 and 1900 eV. Both instruments use soft X-rays as light source, helping to keep beam damage at a minimum in comparison to, e.g., TEM-EELS. They are equipped with high energy-resolving gratings (resolving power at the carbon K-edge: ALS $E/\Delta E \leq 5000$; BESSY II: $E/\Delta E \leq 8000$), a Fresnel zone plate (FZP) providing a spatial resolution of about 40 nm, and phosphor-coated Lucite photomultiplier tubes (PMT) for the detection of transmitted photons. At the ALS, the measurement chamber is filled with He prior to measuring, whereas at BESSY II the measurements are conducted in a vacuum. For energy calibration, the characteristic π resonance peak at 285.2 eV was measured on polystyrene latex spheres (PSLs) prior to each measurement session. As Mn reference materials, $Mn(II)(acac)_2$, $Mn(III)(acac)_3$, and $Mn(IV)O_2$ (acac = acetylacetonate) were used. The data was evaluated using the Interactive Data Language (IDL) widget "Analysis of X-ray microscopy Images and Spectra" (aXis2000) (Hitchcock et al. 2012). Subsequently, cluster analyses were conducted using

the Multivariate ANalysis Tool for Spectromicroscopy software (MANTiS-2.1.01) (Lerotic et al. 2005, Lerotic et al. 2004, Lerotic et al. 2014).

In addition to cluster analysis, non-negative matrix approximation (NNMA) was conducted to extract features while constraining the weightings to be non-negative. The optical density (OD) data can be divided into two matrices, the

5   absorption spectra [μ(E, S); a function of the energy (E) and the set (S) of spectroscopically distinguishable components] and the weighting images [W(S, x, y); a function of the position (x, y) and the set (S) of components] (Mak et al. 2014). The OD can thus be calculated using the equation:

$$OD_{NxP} = \mu_{NxS}\ W_{SxP}$$ Eq. 1

where N is the number of photon energy indices and P the number of pixels (Lerotic et al. 2005). The absorption spectra

10   (μ_{NxS}) are non-negative since the material will only absorb from and never add energy to the transmitted light beam, the weighting maps (W_{SxP}) are non-negative since they are based on the additive nature of the materials with different spectra in the sample (Mak et al. 2014). Since the OD_{NxP} measures the optical density, which is non-negative, it is possible to find non-negative μ_{NxS} and W_{SxP} to satisfy Eq. 1 (Mak et al. 2014). Spectra were calculated using 20,000 iterations, a spectra similarity of 1, a sparseness of 0.5, and a delta error threshold of 0.001. The mathematical background for the sparseness and

15   spectra similarity values can be found in Mak et al. (2014). The spectra were obtained using the three previously measured reference spectra of Mn(II)(acac)$_2$, Mn(III)(acac)$_3$, and Mn(IV)O$_2$, limited to the energy range between 635 and 660 eV, and an additional spectrum of Pt, since Pt is deposited on top of the sample, as initial spectra for the calculation. The Pt spectrum was obtained previously from a sample using cluster analysis, and was also limited to the energy range between 635 and 660 eV.

20   **3 Results and discussion**

The oxidation states of the Mn oxyhydroxide minerals were investigated performing stack scans across the L-edge absorption energy of Mn (635-660 eV). Manganese has three oxidation states in nature, Mn^{2+}, Mn^{3+}, and Mn^{4+}. Even though Mn$^{2+/3+/4+}$ have their main absorption edges at different energies, each oxidation state shows a combination of several individual absorption edges, which are formed by a combination of absorption edges at slightly different energies

25   (multiplets). These multiplets reflect the different binding energies (Cramer et al. 1991, Gilbert et al. 2003, Nesbitt and Banerjee 1998). However, for each oxidation state the absorption at a certain energy (Mn^{2+} ~ 639.7 eV, Mn^{3+} ~ 641.35 eV, Mn^{4+} ~ 643.05 eV) is predominant, so that the oxidation states can be distinguished from each other (Pecher et al. 2003). Findings of reduced Mn around holes within the sample were first interpreted as a sign for reduction of Mn by organics, which had previously filled those cavities, especially since some cavities are lined with C-rich material. However, since the

30   samples are irregularly thinned out, further observations revealed that all thinner parts of the sample consistently showed a higher share of reduced Mn in the spectrum. This is also in agreement with the lower oxidation state around cavities, since

Geoscientific
Instrumentation
Methods and
Data Systems
Discussions
Open Access

by cutting a cavity at an angle, the material is thinner around cavity edges as well. This is shown in detail for sample AR14-J01 from Saudi Arabia (Fig. 1):
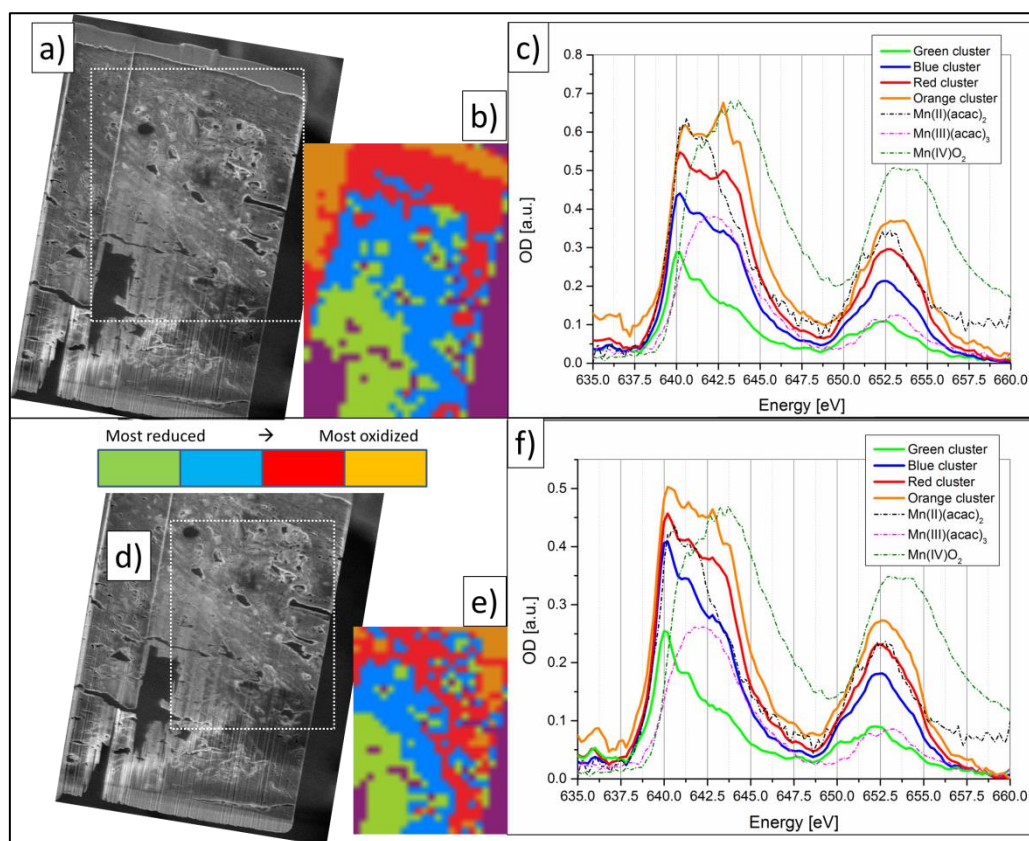
Figure 2: This figure is subdivided into two segments, the upper and the lower part. While a)-c), the upper row, present a cluster analysis conducted on a large area, within which the spectra in the thickest part show the most oxidized Mn signal, this area also partially includes sample material with light transmission of <14 %, thus the data might not be fully reliable. In contrast, d)-f), the lower row, present a cluster analysis on the area with an OD<2 to avoid the possibility of nonlinearity at high OD values. Now, the image shows almost no oxidized material (orange) anymore since the sample is too thin in this area. Images a) and d): SEM image of sample AR14-J01. White dashed squares: area measured by STXM-NEXAFS. Images b) and e): cluster analysis plots of the spectra obtained from the areas marked in a) and d), respectively. The dark purple areas represent the background spectra (no sample in the light beam) and are not shown in c) and f). Image b): the upper part of the sample, where the wedge is thickest, and the right part, which was thinned less, fall into the same cluster with the highest Mn^{4+} and lowest Mn^{2+} fraction (orange cluster). Image e): the sample becomes thicker and the oxidation states higher towards the upper right corner. Images c) and f): Spectra of the areas shown in a) and d), including also three reference spectra of Mn. Images b) and c) were obtained from the area marked in white in image a), images e) and f) were obtained from the area marked in white in image d).

We conducted a cluster analysis (k-means, Euclidian distances) on the sample area investigated by X-ray microspectroscopy (Fig. 2 a) utilizing the software MANTiS. We chose to set k=5 after comparing different signature outcomes using several different k values, since this value seemed to provide the scientifically most meaningful results. Several clusters, defined as pixels with similar absorption spectra, were found (Fig. 2 b). To exclude a cluster pattern based on other element occurrences

or their changing mass fractions, the energy range to conduct the clustering on was limited to the range where the Mn L_2- and L_3-edges absorb (635-660 eV). The spectra of these clusters (Fig. 2 c and f) were smoothed using a three value running mean. For sample AR14-J01, it can be observed that the clusters, and thus also the oxidation states, do not follow any features that can be observed in the SEM image. One can rather see that the upper part of the sample (where the wedge is

5   thickest) and the left part, which was thinned less, fit into the same cluster, with the highest share of Mn^{4+} and the lowest share of Mn^{2+} (Fig. 2 b, c). The oxidation states form concentric circles around the artificial hole (sample thickness = 0), the lowest oxidation state present in the inner circle, higher oxidation state the outer circles.

Due to non-linearities upon very high ODs, we evaluated the OD using the optical density mapping tool of the program MANTiS at 642.4 eV. Due to the split and wedge-shaped thin-out of this sample, several areas had an OD of up to 3. Thus,

10   the evaluated stack area was cropped to exclude the high OD areas, in order to obtain information only from the sample areas that provide light transmission of at least 14 % in the energy range of the Mn absorption, thus an OD of ≤2 (Fig. 2 d). We conducted another cluster analysis on this cropped sample area, which excluded sample material with an OD>2 and was thus limited to material sufficiently transparent for the light used. Several clusters were found, which, however, still follow the thickness of the sample (Fig. 2 e, f). Sample AR14-J01 had been thinned out from the bottom left upwards to the right corner

15   (Fig. 1). At the sites where the sample is thinnest, the Mn^{2+} peak fraction dominates. The thicker the sample becomes, the higher is the Mn^{4+} share in the spectrum (Figs. 1 and 2). A possible explanation for the change of the Mn oxidation states correlating with the sample thickness is that for very thin samples the fraction of the surface layer (nm range) to the total measured sample volume is very high. A high surface fraction is equivalent to a high potential for beam damage. The phenomenon of increasing oxidation states ($Mn^{2+} \rightarrow Mn^{3+} \rightarrow Mn^{4+}$) from the thinnest to the thickest areas was clearly

20   observed in those samples that had strong differences in thickness, while it was less clear for other samples, which had been thinned out more homogenously. This suggests that surface modifications during preparation are in fact responsible for the oxidation state variations found.

The Mn oxidation state distribution indicates that a modification of the material had taken place. The exposure of the samples to the incident X-ray beam using STXM-NEXAFS would be a possible source for the oxidation state reduction, if

25   excessive doses had been used (Süzer 2000). This is, however, not the case here, since our reference spectra showed no sign of changes. Furthermore, experiments were conducted to search for differences between sequences of scans on the same area (e.g. successive stacks on the same sample area). Since no difference could be observed, we can rule out this artifact source. Moreover, successful X-ray microspectroscopy measurements have been performed of materials with different Mn oxidation states before (Bargar et al. 2001, Glasauer et al. 2006, Pecher et al. 2000, Pecher et al. 2003, Tebo et al. 2004, Toner et al.

30   2005). Thus, the radiation damage affecting the oxidation states of Mn was most likely introduced during the sample preparation procedure. While STXM-NEXAFS measurements are conducted with energies in the eV range, FIB preparation and SEM imaging utilize energies in the keV range. To verify whether a layer of modified material is actually distributed homogeneously on the surface of the sample, and to show the contribution of an individual spectrum to each pixel, we conducted NNMA. Figure 3 e) shows the spectra obtained by NNMA analysis, excluding the Pt spectrum. The three spectra

(Fig. 3 e) and their distributions (Fig. 3 a-c) provide additional information to that presented in Fig. 2. One can observe a Mn^{2+}-rich spectrum (spectrum "a", shown in blue in Fig 3 d and e), which is only present as a specific feature within the sample (distribution shown in Fig 3 a and d), a Mn^{4+}-rich spectrum (spectrum "b", shown in green in Fig 3 d and e), which is only present within the very thick parts of the sample (distribution shown in Fig 3 b and d), and a $Mn^{2+/3+}$-rich spectrum with

5   broad peaks (spectrum "c", shown in red in Fig 3 d and e), which can be found homogeneously distributed over the whole sample (distribution shown in Fig 3 c and d) and which is very likely to present the modified material on the sample surface. This confirms our assumptions that (i) there is some sort of surface modification (spectrum "c") that is present on the entire sample surface and has broad peaks, and that (ii) actual features can be observed and visualized below this modified surface (spectrum "a"), but only in areas that are not too thin (such as the lower left part of the sample), and that (iii) spectra similar

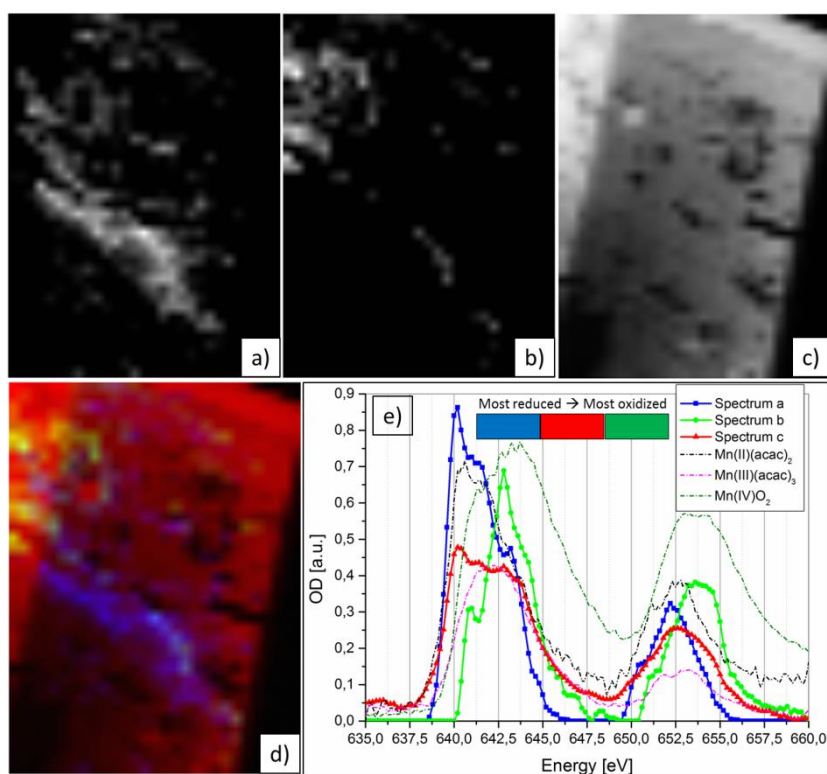10   to Mn^{4+}, thus non-reduced Mn, can only be found in thicker areas (spectrum "b").

Figure 3: Non-negative matrix approximation (NNMA) of sample AR14-J01. Images a), b), and c) show the spatial distribution of the spectra "a" (Mn^{2+}-rich), "b" (Mn^{4+}-rich), and "c" ($Mn^{2+/3+}$-rich) plotted in e). The names in image e) correspond to the name of
15   **the image showing the spectrum distribution. Also plotted in e) are the reference spectra of the three Mn oxidation states. Image d) presents an overlay of the distributions of the materials showing the three spectra (a) in blue, b) in green, c) in red), corresponding to the colors chosen in image e).**

4 Conclusions

In this study, we found that the Mn oxidation states investigated using STXM-NEXAFS were modified during the sample preparation procedure by reducing Mn^{4+} to $Mn^{2+/3+}$, especially in the upper surface layers of the FIB slice. Original features of the Mn oxidation states can possibly be obtained using NNMA, where a general spectrum of the modified surface material

5   can be subtracted from the pixel stacks to reveal the original spectra of the less-modified features below this layer. However, it cannot be verified that those Mn oxidation states have not been, or to which degree they have been, modified, or whether peaks did shift.

Overall, we found that artifacts are produced during the preparation of the samples by FIB and monitoring by SEM, which create a high degree of uncertainty for oxidation state analyses. This study supplies a clearer picture on the type of artifacts

10   created, which provides the possibility to check this carefully in follow-up studies. As there is at this time no alternative to FIB as sample preparation technique to produce intact ultra-thin slices of rock samples, one needs to be aware of these problems and choose preparation parameters that help to keep damage to a minimum. To reduce or minimize the damaged area, the preparation procedure could be conducted using lower voltages during preparation with the FIB and SEM or, if available, a cryo-FIB (Bassim et al. 2012). However, it is left to further studies to investigate whether oxidation states can

15   indeed be kept unchanged using more gentle preparation approaches.

References

Balcells, L., L. Abad, H. Rojas & B. Martinez (2008) Material damage induced by nanofabrication processes in manganite
25   thin films. *Nanotechnology,* 19**,** 135307.
Bargar, J., B. Tebo, K. Pecher, D. McCubbery, V. Chiu & B. Tonner. 2001. Manganese Oxide Biomineralization by Spores of the Marine Bacillus sp. Strain SG-1. In *AGU Fall Meeting Abstracts*.
Bassim, N., B. De Gregorio, A. Kilcoyne, K. Scott, T. Chou, S. Wirick, G. Cody & R. Stroud (2012) Minimizing damage during FIB sample preparation of soft materials. *Journal of Microscopy,* 245**,** 288-301.
30   Bender, H. & P. Roussel (1997) Cross-sectional transmission electron microscopy and focused ion beam study of advanced silicon devices. *Microscopy of Semiconducting Materials 1997***,** 465-468.
Cairney, J. M., R. D. Smith & P. R. Munroe (2000) Transmission electron microscope specimen preparation of metal matrix composites using the focused ion beam miller. *Microscopy and Microanalysis,* 6**,** 452-462.
Cerva, H. & G. Hobler. 1993. Depth of amorphized ion implanted silicon zones predicted from point defect density
35   calculations and TEM cross sections. In *Conference Series-Institute of Physics*, 133-133. IOP Publishing LTD.

Cosmidis, J. & K. Benzerara (2014) Soft X-ray scanning transmission spectromicroscopy. *Biomineralization Sourcebook: characterization of biominerals and biomimetic materials*, 115-133.

Cramer, S., F. DeGroot, Y. Ma, C. Chen, F. Sette, C. Kipke, D. Eichhorn, M. Chan & W. Armstrong (1991) Ligand field strengths and oxidation states from manganese L-edge spectroscopy. *Journal of the American Chemical Society,* 113, 7937-7940.

Egerton, R., P. Li & M. Malac (2004) Radiation damage in the TEM and SEM. *Micron,* 35, 399-409.

Follath, R., J. S. Schmidt, M. Weigand & K. Fauth (2010) The X-ray microscopy beamline UE46-PGM2 at BESSY. *Sri 2009: The 10th International Conference on Synchrotron Radiation Instrumentation. Eds: R. Garrett, I. Gentle, K. Nugent, S. Wilkins*, 323-326.

Garvie, L. A. J., D. M. Burt & P. R. Buseck (2008) Nanometer-scale complexity, growth, and diagenesis in desert varnish. *Geology,* 36, 215-218.

Giannuzzi, L. A., R. Geurts & J. Ringnalda (2005) 2 keV Ga+ FIB milling for reducing amorphous damage in silicon. *Microscopy and Microanalysis,* 11, 828.

Gilbert, B., B. Frazer, A. Belz, P. Conrad, K. Nealson, D. Haskel, J. Lang, G. Srajer & G. De Stasio (2003) Multiple scattering calculations of bonding and X-ray absorption spectroscopy of manganese oxides. *The Journal of Physical Chemistry A,* 107, 2839-2847.

Glasauer, S., S. Langley, T. Beveridge, S. Fakra, T. Tyliszczak, D. Shuh, M. Boyanov & K. Kemner. 2006. The Internalization of Iron and Manganese as Discrete Particles During the Bioreduction of Fe (III) and Mn (IV) by a Dissimilatory Metal-Reducing Bacterium. In *AGU Fall Meeting Abstracts*.

Guttmann, P. & C. Bittencourt (2015) Overview of nanoscale NEXAFS performed with soft X-ray microscopes. *Beilstein journal of nanotechnology,* 6, 595.

Halada, G., C. Clayton & D. Lindsley (1988) Evidence of photoreduction in thermal oxides formed on chromium. *Materials Science and Engineering: A,* 103, L5-L7.

Henderson, R. & R. M. Glaeser (1985) Quantitative analysis of image contrast in electron micrographs of beam-sensitive crystals. *Ultramicroscopy,* 16, 139-150.

Hitchcock, A., P. Hitchcock, C. Jacobsen, C. Zimba, B. Loo, E. Rotenberg, J. Denlinger & R. Kneedler (2012) aXis 2000—Analysis of X-ray Images and Spectra. *McMaster University: Hamilton, ON, Canada*.

Jamison, R., A. Mardinly, D. Susnitzky & R. Gronsky (2000) Effects of ion species and energy on the amorphization of Si during FIB TEM sample preparation as determined by computational and experimental methods. *Microscopy and Microanalysis-New York-,* 6, 526-527.

Kilcoyne, A. L. D., T. Tyliszczak, W. F. Steele, S. Fakra, P. Hitchcock, K. Franck, E. Anderson, B. Harteneck, E. G. Rightor, G. E. Mitchell, A. P. Hitchcock, L. Yang, T. Warwick & H. Ade (2003) Interferometer-controlled scanning transmission X-ray microscopes at the Advanced Light Source. *Journal of Synchrotron Radiation,* 10, 125-136.

Knotek, M. & P. J. Feibelman (1978) Ion desorption by core-hole Auger decay. *Physical Review Letters,* 40, 964.

Krinsley, D., R. Dorn & N. Tovey (1995) Nanometer-scale layering in rock varnish: implications for genesis and paleoenvironmental interpretation. *The Journal of Geology,* 103, 106-113.

Lerotic, M., C. Jacobsen, J. Gillow, A. Francis, S. Wirick, S. Vogt & J. Maser (2005) Cluster analysis in soft X-ray spectromicroscopy: finding the patterns in complex specimens. *Journal of Electron Spectroscopy and Related Phenomena,* 144, 1137-1143.

Lerotic, M., C. Jacobsen, T. Schäfer & S. Vogt (2004) Cluster analysis of soft X-ray spectromicroscopy data. *Ultramicroscopy,* 100, 35-57.

Lerotic, M., R. Mak, S. Wirick, F. Meirer & C. Jacobsen (2014) MANTiS: a program for the analysis of X-ray spectromicroscopy data. *Journal of synchrotron radiation,* 21, 1206-1212.

Li, J. & P. Liu. 2017. Important Factors to Consider in FIB Milling of Crystalline Materials. In *Characterization of Minerals, Metals, and Materials 2017*, 329-336. Springer.

Li, P. (2003) Electron irradiation damage to organic light-emitting materials. *MSc thesis, University of Alberta, Canada*.

Mak, R., M. Lerotic, H. Fleckenstein, S. Vogt, S. M. Wild, S. Leyffer, Y. Sheynkin & C. Jacobsen (2014) Non-negative matrix analysis for effective feature extraction in X-ray spectromicroscopy. *Faraday discussions,* 171, 357-371.

Mardinly, J. & D. W. Susnitzky (1998) Transmission electron microscopy of semiconductor based products. *MRS Online Proceedings Library Archive,* 523.

Mayer, J., L. A. Giannuzzi, T. Kamino & J. Michael (2007) TEM sample preparation and FIB-induced damage. *MRS bulletin,* 32**,** 400-407.

Michael, J. (2006) Gallium phase formation in Cu during 30kV Ga+ FIB milling. *Microscopy and Microanalysis,* 12**,** 1248.

Moffet, R. C. (2011) Scanning transmission X-ray microscopy: Applications in atmospheric aerosol research. *Lawrence Berkeley National Laboratory*.

Nesbitt, H. & D. Banerjee (1998) Interpretation of XPS Mn (2p) spectra of Mn oxyhydroxides and constraints on the mechanism of MnO2 precipitation. *American Mineralogist,* 83**,** 305-315.

Pallecchi, I., L. Pellegrino, E. Bellingeri, A. Siri, D. Marré & G. Gazzadi (2008) Investigation of FIB irradiation damage in La 0.7 Sr 0.3 MnO 3 thin films. *Journal of Magnetism and Magnetic Materials,* 320**,** 1945-1951.

Pecher, K., E. Kneedler, J. Rothe, G. Meigs, T. Warwick, K. Nealson & B. Tonner. 2000. Charge state mapping of mixed valent iron and manganese mineral particles using Scanning Transmission X-ray Microscopy (STXM). In *AIP Conference Proceedings*, 291-300. AIP.

Pecher, K., D. McCubbery, E. Kneedler, J. Rothe, J. Bargar, G. Meigs, L. Cox, K. Nealson & B. Tonner (2003) Quantitative charge state analysis of manganese biominerals in aqueous suspension using scanning transmission X-ray microscopy (STXM). *Geochimica et Cosmochimica Acta,* 67**,** 1089-1098.

Prenitzer, B., L. Giannuzzi, K. Newman, S. Brown, R. Irwin, F. Stevie & T. Shofner (1998) Transmission electron microscope specimen preparation of Zn powders using the focused ion beam lift-out technique. *Metallurgical and Materials Transactions A,* 29**,** 2399-2406.

Rajsiri, S., B. Kempshall, S. Schwarz & L. Giannuzzi (2002) FIB damage in silicon: Amorphization or redeposition. *Microsc. Microanal,* 8.

Reimer, L. 1975. Review of the radiation damage problem of organic specimens in electron microscopy. New York: In: Siegel, B.M. and Beaman, D.R. (Eds.), Physical Aspects of Electron Microscopy and Microbeam Analysis, Wiley.

Roof, S. & C. Callagan (2003) The climate of Death Valley, California. *Bulletin of the American Meteorological Society,* 84**,** 1725.

Rubanov, S. & P. Munroe (2001) Investigation of the structure of damage layers in TEM samples prepared using a focused ion beam. *Journal of materials science letters,* 20**,** 1181-1183.

--- (2004a) FIB-induced damage in silicon. *Journal of Microscopy,* 214**,** 213-221.

Rubanov, S. & P. R. Munroe (2004b) FIB-induced damage in silicon. *Journal of Microscopy,* 214**,** 213-221.

Sherman, D. M. (2005) Electronic structures of iron (III) and manganese (IV)(hydr) oxide minerals: Thermodynamics of photochemical reductive dissolution in aquatic environments. *Geochimica et Cosmochimica Acta,* 69**,** 3249-3255.

Siemons, W., C. Beekman, J. Fowlkes, N. Balke, J. Tischler, R. Xu, W. Liu, C. Gonzales, J. Budai & H. Christen (2014) Focused-ion-beam induced damage in thin films of complex oxide BiFeO3. *APL Materials,* 2**,** 022109.

Susnitzky, D. W. & K. D. Johnson (1998) Focused ion beam (FIB) milling damage formed during TEM sample preparation of silicon. *Microscopy and Microanalysis-New York-,* 4**,** 656-657.

Süzer, Ş. (2000) XPS investigation of X-ray-induced reduction of metal ions. *Applied Spectroscopy,* 54**,** 1716-1718.

Tebo, B. M., J. R. Bargar, B. G. Clement, G. J. Dick, K. J. Murray, D. Parker, R. Verity & S. M. Webb (2004) Biogenic manganese oxides: Properties and mechanisms of formation. *Annual Review of Earth and Planetary Sciences,* 32**,** 287-328.

Tebo, B. M., H. A. Johnson, J. K. McCarthy & A. S. Templeton (2005) Geomicrobiology of manganese (II) oxidation. *TRENDS in Microbiology,* 13**,** 421-428.

Toner, B., S. Fakra, M. Villalobos, T. Warwick & G. Sposito (2005) Spatially resolved characterization of biogenic manganese oxide production within a bacterial biofilm. *Applied and environmental microbiology,* 71**,** 1300-1310.

Weigand, M. 2015. *Realization of a new magnetic scanning X-ray microscope and investigation of Landau structures under pulsed field excitation*. Cuvillier Verlag.